Inductive Power Transfer Systems for Bus-Stop-Powered Electric Vehicles

Authors:

Chung-Chuan Hou, Kuei-Yuan Chang

Date Submitted: 2019-01-07

Keywords: bus-stop-powered, electric vehicles, inductive power transfer

Abstract:

This study presents an inductive power transfer (IPT) system for electric vehicles (EVs) based on EE-shaped ferrite cores. The issues of the IPT system such as efficiency, air gap, displacement, dislocation, and motion are discussed. Furthermore, finite element analysis software is utilized to simulate the IPT system operated under large air gap conditions. Simulation and measurement results are presented to validate the performance of the proposed scheme and meet the requirements for bus-stop-powered EVs.

Record Type: Published Article

Submitted To: LAPSE (Living Archive for Process Systems Engineering)

Citation (overall record, always the latest version):	LAPSE:2019.0018
Citation (this specific file, latest version):	LAPSE:2019.0018-1
Citation (this specific file, this version):	LAPSE:2019.0018-1v1

DOI of Published Version: https://doi.org/10.3390/en9070512

energies

MDPI

Letter

Inductive Power Transfer Systems for Bus-Stop-Powered Electric Vehicles

Chung-Chuan Hou * and Kuei-Yuan Chang

Department of Electrical Engineering, Chung Hua University, Hsinchu 30012, Taiwan; f26714317@gmail.com
* Correspondence: bird@chu.edu.tw; Tel.: +886-3-518-6351

Academic Editor: Chunhua Liu
Received: 20 February 2016; Accepted: 20 June 2016; Published: 30 June 2016

Abstract: This study presents an inductive power transfer (IPT) system for electric vehicles (EVs) based on EE-shaped ferrite cores. The issues of the IPT system such as efficiency, air gap, displacement, dislocation, and motion are discussed. Furthermore, finite element analysis software is utilized to simulate the IPT system operated under large air gap conditions. Simulation and measurement results are presented to validate the performance of the proposed scheme and meet the requirements for bus-stop-powered EVs.

Keywords: inductive power transfer; bus-stop-powered; electric vehicles

1. Introduction

As the air pollution problems caused by gasoline-powered vehicles have become more and more serious, electric vehicles (EVs) [1–3] or hybrid EVs have been regarded as good solutions and gained increasing attention. However, the batteries used in EVs or hybrid EVs have some significant disadvantages, such as high cost and heaviness, limited capacitance and charging/discharging cycles, and long charging time, etc. The roadway-powered EVs [4–8] scheme has therefore been discussed to reduce the battery capacitance and to extend the driving range. This study would like to furthermore present the inductive power transfer (IPT) system [9–13] for bus-stop-powered EVs [14] with much less cost than the roadway-powered EVs system.

Figure 1 shows the IPT system for bus-stop-powered EVs or hybrid EVs. The active front-end (AFE) converter is utilized as interface between the AC voltage grid and DC voltage grid. The advantages of the AFE converter are bidirectional power flow and low total harmonic distortion (THD) of the line current. The primary side of the IPT system is DC-AC H-bridge inverters. The multi-H-bridge inverters are utilized to increase the transfer power and efficiency of the IPT system. The secondary side of the IPT system is a pick-up coil and receiver built in the EVs or hybrid EVs. The IPT receiver is utilized to charge up battery or supply power to motor through the inverter. The IPT system for moving EVs or hybrid EVs is convenient for charging up battery and could also extend driving range. Furthermore, the position regulation sensors of the IPT system are utilized to control the operation of multi-H-bridge inverters and improve the efficiency of the IPT system.

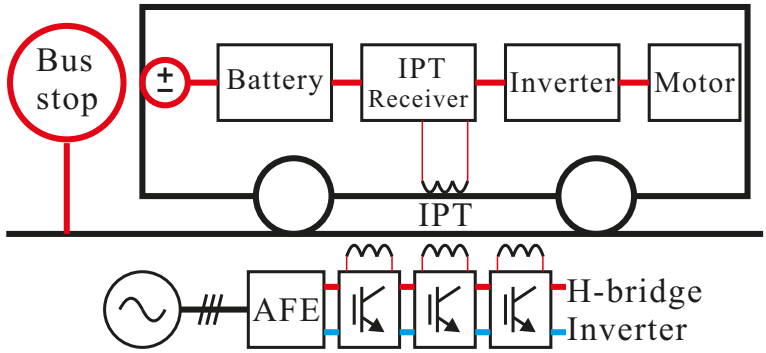

Figure 1. Inductive power transfer system for bus-stop-powered EVs or hybrid EVs.

2. Inductive Power Transfer System

Figure 2 shows the simplified IPT system based on EE-shaped ferrite cores for bus-stop-powered EVs or hybrid EVs. As shown in Figure 2a, the DC bus voltage is V_{dc}, the DC-AC H-bridge inverter is utilized to generate the high frequency square wave voltage V_{in}. The EE-shaped ferrite cores are utilized to transfer the power to secondary side load (by pick-up coil and receiver). The primary inductance and secondary inductance are L_p and L_s. The mutual inductance is M (=L_m). The coupling coefficient (k) is defined as in (1):

$$k = \frac{M}{\sqrt{L_P L_S}} \tag{1}$$

As shown in Figure 2b, the dimensions of the EE-shaped cores are A (80 mm), B (38 mm), C (20 mm), D (28 mm), E (59 mm), F (20 mm), G (F/2), H (E/2–F/2), and I (A/4–E/4). The material of the EE-shaped cores is 3C90 made by Ferroxcube (New Taipei City, Taiwan, R.O.C.). The relative permeability is 2300 (permeability of free space: $4\pi \times 10^{-7}$ H/m). Figure 2c shows the equivalent circuit of the primary series resonant and secondary parallel resonant (SP) topology IPT system and Figure 2d shows the secondary parallel resonant (P) topology IPT system, respectively.

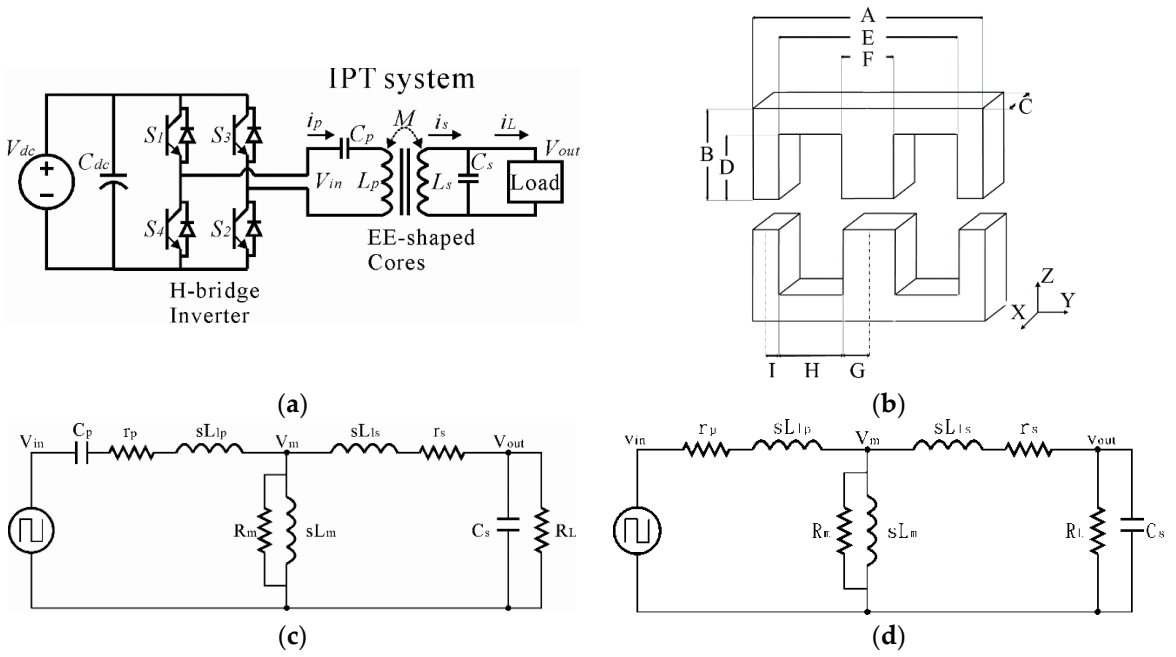

Figure 2. Simplified inductive power transfer system. (**a**) Circuit of the IPT system; (**b**) EE-shaped cores; (**c**) Equivalent circuit of the SP topology; (**d**) Equivalent circuit of the P topology.

The mutual inductance is M (=L_m) and the equivalent resistance of core loss is R_m. The primary and secondary leakage inductances are L_{lp} and L_{ls} as in (2).

$$L_{lp} = (1-\mathrm{k})L_p,\ L_{ls} = (1-\mathrm{k})L_s \tag{2}$$

The primary and secondary resistances are r_p and r_s. The load is simplified as R_L. The primary series resonant capacitor is C_P and the secondary parallel resonant capacitor is Cs. The transfer function of the SP topology IPT system is given as in (3):

$$\frac{v_{out}(s)}{v_{in}(s)} = \frac{s^2 \times C_P \times L_m \times R_L/[R_m \times (R_L + r_S)]}{(1 + \frac{s}{p_H}) \times (1 + \frac{2\zeta_1}{\omega_{n1}}s + \frac{s^2}{\omega_{n1}^2}) \times (1 + \frac{2\zeta_2}{\omega_{n2}}s + \frac{s^2}{\omega_{n2}^2})} \tag{3}$$

The pole (s = $-P_H$) operated at the high frequency domain is as in (4):

$$p_H = R_m \times (\frac{1}{L_{lp}} + \frac{1}{L_{ls}} + \frac{1}{L_m}) \tag{4}$$

The complex-conjugate poles operated at the low frequency domain are as in (5):

$$s = -(\zeta_1 \pm j\sqrt{1-\zeta_1^2})\omega_{n1} \tag{5}$$

where the damping ratio is $\zeta_1 = r_P C_P \omega_{n1}/2$, natural undamped frequency is $\omega_{n1} = \sqrt{1/C_P(L_{lp} + L_m)}$ and resonant frequency is $\omega_{r1} = \sqrt{1-\zeta_1^2}\omega_{n1}$, respectively.

The complex-conjugate poles operated at the middle frequency domain are as in (6):

$$s = -(\zeta_2 \pm j\sqrt{1-\zeta_2^2})\omega_{n2} \tag{6}$$

where the damping ratio is $\zeta_2 = 1/2R_L C_S \omega_{n2}$, natural undamped frequency is $\omega_{n2} = \sqrt{\frac{(1+r_S/R_L)}{C_S(L_{ls} + \frac{L_{lp} \times L_m}{L_{lp}+L_m})}}$ and resonant frequency is $\omega_{r2} = \sqrt{1-\zeta_2^2}\omega_{n2}$, respectively.

According to (3), the transfer function of the IPT system with P topology is reduced as in (7):

$$\frac{v_{out}(s)}{v_{in}(s)} = \frac{s \times L_m \times R_L/(r_P \times (R_L + r_S))}{(1 + \frac{s}{p_L}) \times (1 + \frac{s}{p_H}) \times (1 + \frac{2\zeta_2}{\omega_{n2}}s + \frac{s^2}{\omega_{n2}^2})} \tag{7}$$

The high frequency pole (s = $-P_H$) is as in (4) and the low frequency pole (s = $-P_L$) is as in (8):

$$p_L = r_P/(L_{lp} + L_m) \tag{8}$$

The complex-conjugate poles operated at the middle frequency domain are as in (9):

$$s = -(\zeta \pm j\sqrt{1-\zeta^2})\omega_n \tag{9}$$

where the damping ratio is $\zeta = 1/2R_L C_S \omega_n$, natural undamped frequency is $\omega_n = \sqrt{\frac{(1+r_S/R_L)}{C_S(L_{ls} + \frac{L_{lp} \times L_m}{L_{lp}+L_m})}}$ and resonant frequency is $\omega_r = \sqrt{1-\zeta^2}\omega_n$, respectively.

According to (3) and (7), there are two pairs of resonant poles in the SP topology IPT system and one pair of resonant poles in the P topology IPT system.

3. Frequency Response of the IPT System

The parameters of the IPT system are as follows: the primary inductance and secondary inductance are *Lp* (325 μH) and *Ls* (325 μH). The primary series resonant capacitor is C_P (0.2 μF) and the secondary parallel resonant capacitor is *Cs* (0.2 μF). The resistances r_p and r_s are 0.72 Ω. The load resistance R_L is 100 Ω.

Figure 3 shows the frequency response of the IPT system based on EE-shaped cores with varied air gap (fsw: 10–100 kHz). In SP topology, the resonant frequencies ω_{r1} and ω_{r2} move to each other as the air gap is increased as shown in Figure 3a. In P topology, the resonant peak value is decreased as the air gap is increased as shown in Figure 3b. Therefore, the SP topology is suitable for a large air gap IPT system and the P topology suits a small air gap IPT system. The coupling coefficient and resonant frequency of the IPT system with varied air gap are given in Table 1.

Table 1. Coupling coefficient and resonant frequency of the IPT system with varied air gap.

Gap	5 mm	10 mm	20 mm
L_{lp}	217.7 μH	237.2 μH	282.7 μH
L_{ls}	217.7 μH	237.2 μH	282.7 μH
L_m	107.3 μH	87.8 μH	42.3 μH
k	0.33	0.27	0.13
ω_{r1}	15 kHz	17 kHz	20 kHz
ω_{r2}	23 kHz	22 kHz	20 kHz
ω_r	20 kHz	20 kHz	20 kHz

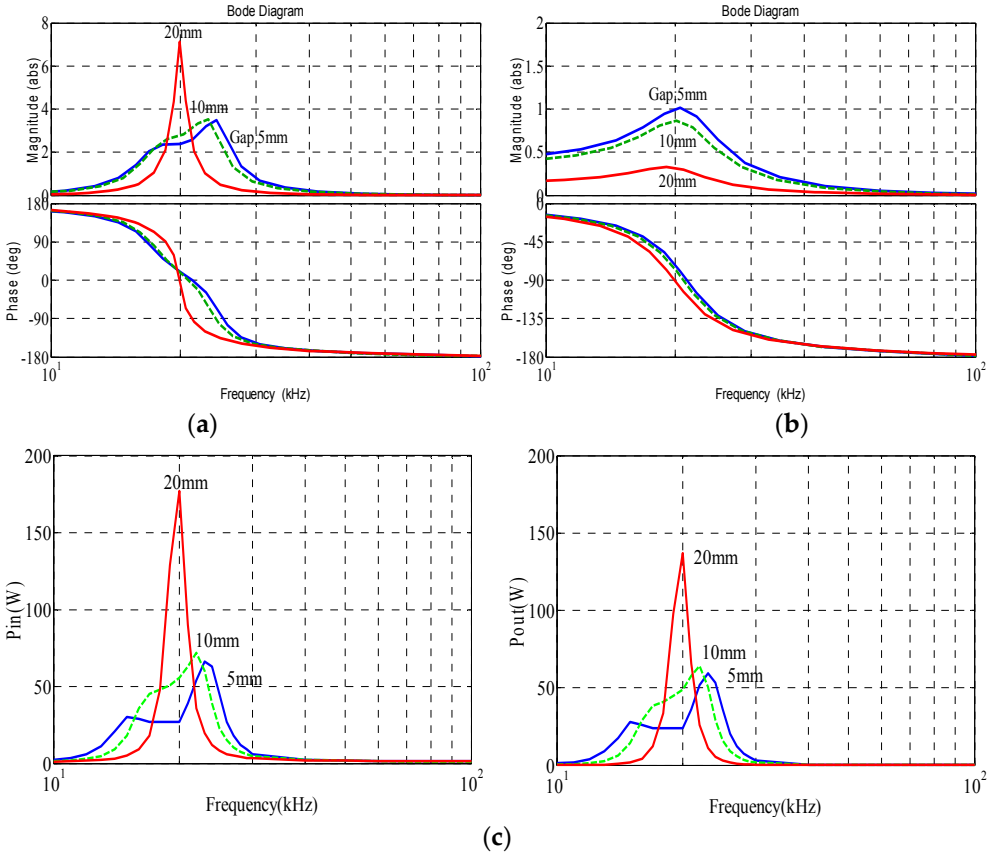

Figure 3. *Cont.*

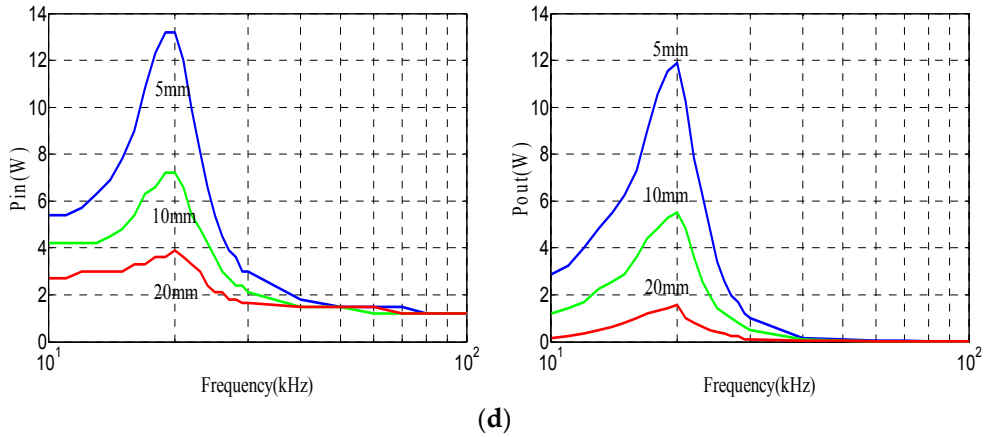

Figure 3. Frequency response of the IPT system based on EE-shaped cores with varied air gap. (**a**) SP topology (MATLAB); (**b**) P topology (MATLAB); (**c**) Input power and output power of SP topology (test results; V_{dc}: 30 V); (**d**) Input power and output power of P topology (test results; V_{dc}: 30 V).

Figure 3c shows the input power and output power of the SP topology IPT system with varied air gap (test results; V_{dc}: 30 V). The resonant frequencies of the IPT system are 15 kHz (ω_{r1}) and 23 kHz (ω_{r2}) under air gap 5 mm, 17 kHz (ω_{r1}) and 22 kHz (ω_{r2}) under air gap 10 mm, and 20 kHz ($\omega_{r1,2}$) under air gap 20 mm, respectively. The input power and output power are increased and the efficiency is decreased as air gap increased. The measurement results of the SP topology IPT system are given in Table 2. Figure 3d shows the input power and output power of the P topology IPT system with varied air gap (test results; V_{dc}: 30 V). The input power, output power, and the efficiency are decreased as air gap increased. The measurement results of the P topology IPT system are given in Table 2. As shown in Figure 3, the measurement results agree with the simulation results produced by using MATLAB.

Table 2. Input power, output power, and efficiency of the IPT system.

	Gap	**5 mm ω_{r1}: 15 kHz**	**5 mm ω_{r2}: 23 kHz**	**10 mm ω_{r1}: 17 kHz**	**10 mm ω_{r2}: 22 kHz**	**20 mm $\omega_{r1,2}$: 20 kHz**
SP TOPOLOGY	Input power	30 W	66 W	45 W	72 W	177 W
	Output power	28 W	59.3 W	38.4 W	64 W	136.9 W
	Efficiency	94%	90%	85%	89%	77%
	Gap	**5 mm ω_r: 20 kHz**		**10 mm ω_r: 20 kHz**		**20 mm ω_r: 20 kHz**
P TOPOLOGY	Input power	13.2 W		7.2 W		3.9 W
	Output power	11.9 W		5.5 W		1.6 W
	Efficiency	90%		77%		40%

4. Simulation and Experimental Results

Figure 4 shows the prototype of measurement for the P topology IPT system operated at small air gap. The multi-H-bridge inverters are utilized to increase the transfer power and efficiency of the P topology IPT system as shown in Figure 4a. The X-Z table and controller are utilized to move the pick-up coil and IPT receiver along the *X*-axis as shown in Figure 4b. The parameters of measurement are the same as Section 3. The issues of the IPT system [13] such as efficiency, air gap (*Z*-axis), displacement (*X*-axis), dislocation (*Y*-axis), and motion (*X*-axis) are discussed as follow:

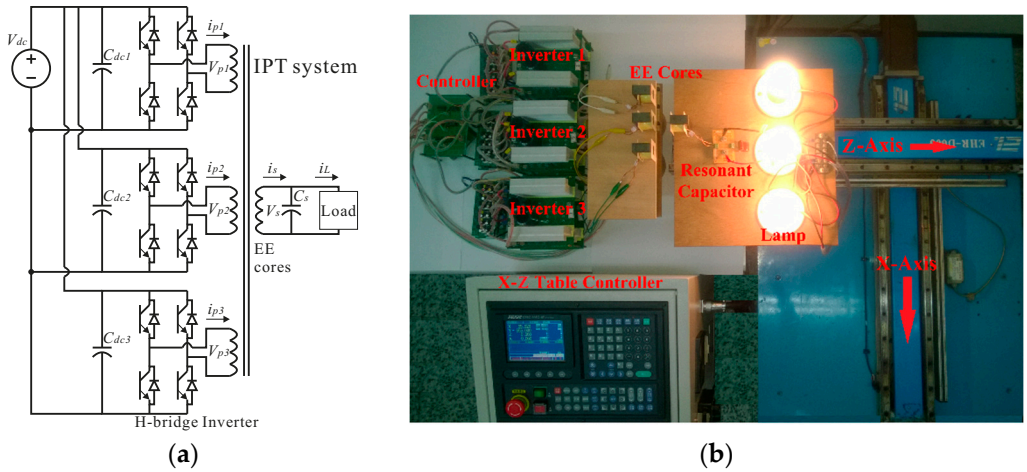

Figure 4. Prototype of measurement for the P topology IPT system. (**a**) multi-H-bridge inverters (**b**) prototype of measurement.

4.1. Air Gap

Figure 5 shows the efficiency, input power, and output power of the P topology IPT system based on one H-bridge inverter with varied air gap and operating frequency. The switching frequency (fsw) is from 10 kHz to 100 kHz. As shown in Figure 5a, for various operating frequencies, the IPT system exhibits superior performance at the resonant frequency (20 kHz). The efficiency of the IPT system is decreased by increased operating frequency. Table 3 shows the efficiency, input power, and output power of the P topology IPT system at 20 kHz. The maximum efficiency of the IPT system is 93% at air gap 5 mm. Figure 5b shows the efficiency, input power, and output power of the IPT system with varied air gap from 5 mm to 65 mm (fsw: 20 kHz). The efficiency, input power, output power, and power loss of the IPT system are 50.9%, 49.5 W, 25.2 W, and 24.3 W (gap: 21 mm). The performances of the P topology IPT system are increased by a decreased air gap.

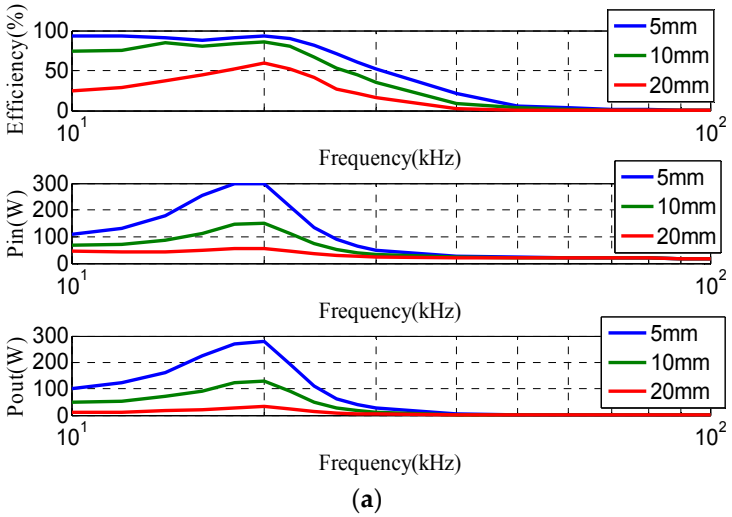

Figure 5. *Cont.*

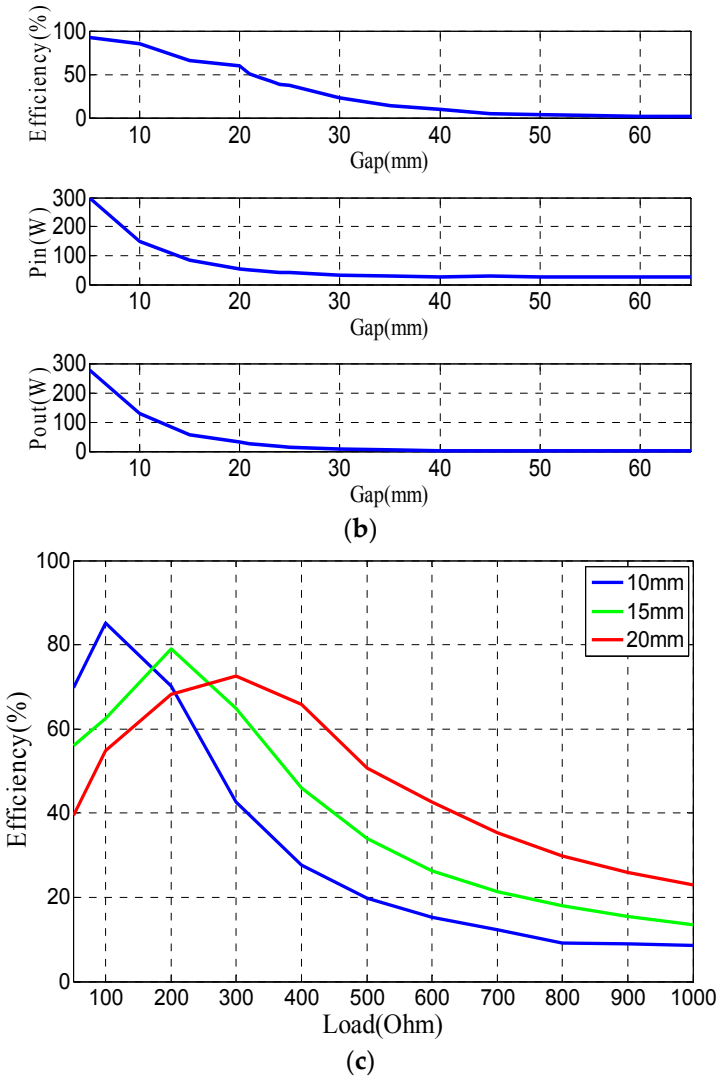

Figure 5. Efficiency, input power, and output power of the P topology IPT system with varied air gap and frequency (V_{dc}: 150 V; R_L: 100 Ω). (**a**) Efficiency, input power, and output power; (**b**) Varied air gap from 5 mm to 65 mm (20 kHz); (**c**) Varied load (20 kHz).

Table 3. Efficiency, input power, and output power of the IPT system with varied air gap at 20 kHz.

Air Gap (mm)	5	10	20
Efficiency	93%	85%	60%
Input Power(W)	300	150	54
Output Power(W)	278	128	32

Figure 5c shows the efficiency of the P topology IPT system with varied load 50–1000 Ω (V_{dc}: 150 V; fsw: 20 kHz). The efficiency, input power, and output power of the P topology IPT system are 85%, 150 W, and 128 W under load 100 Ω (gap: 10 mm). The efficiency, input power, and output power of the P topology IPT system are 79%, 150 W, and 119 W under load 200 Ω (gap: 15 mm). The efficiency, input power, and output power of the P topology IPT system are 72%, 120 W, and 86 W under load 300 Ω (gap: 20 mm). The efficiency of the P topology IPT system is affected by the load and air gap.

4.2. Displacement

The displacement is defined as moving along the *X*-axis. Figure 6 shows the displacement effect of the IPT system based on one H-bridge inverter with varied air gap from 5 mm to 40 mm (fsw: 20 kHz). Table 4 shows the efficiency, input power, output power, and power loss of the IPT system. Table 4 is for displacements of 10 mm and 20 mm, respectively. The performances of the IPT system are increased by decreased displacement.

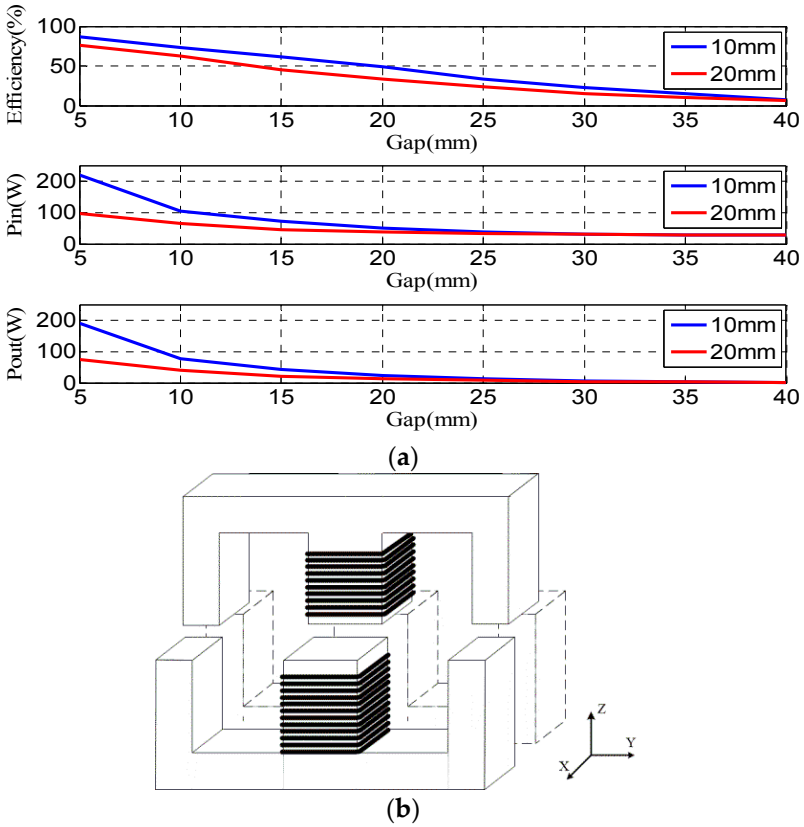

Figure 6. Displacement effect of the IPT system with varied air gap from 5 mm to 40 mm (V_{dc}: 150 V; fsw: 20 kHz). (**a**) Efficiency, input power; and output power (**b**) Displacement.

Table 4. Displacement effect of the IPT system with varied air gap from 5 mm to 40 mm (fsw: 20 kHz).

Displacement	Air Gap (mm)	5	10	15	20	25	30	35	40
Displacement: 10 mm	Efficiency	86.8%	73.2%	61.4%	49.5%	33.3%	22.9%	14.8%	7.4%
	Input power (W)	219	105	72	49.5	37.5	31.5	28.5	27
	Output power (W)	191.1	77.2	44.1	24.5	12.5	7.2	4.2	2
Displacement: 20 mm	Efficiency	76.3%	62.7%	45.4%	33.3%	24.2%	15.0%	10.6%	6.0%
	Input power (W)	97.5	64.5	46.5	37.5	33	30	27	27
	Output power (W)	74.4	40.5	21.1	12.5	8	4.5	2.9	1.6

4.3. Dislocation

The dislocation is defined as moving along the *Y*-axis. Figure 7 shows the dislocation effect of the IPT system based on one H-bridge inverter with varied air gap from 5 mm to 40 mm (fsw: 20 kHz). The dislocation effect of the IPT system with varied air gap is given in Table 5. Table 5 is for dislocations of 10 mm and 20 mm, respectively. The performances of the IPT system are increased by decreased dislocation.

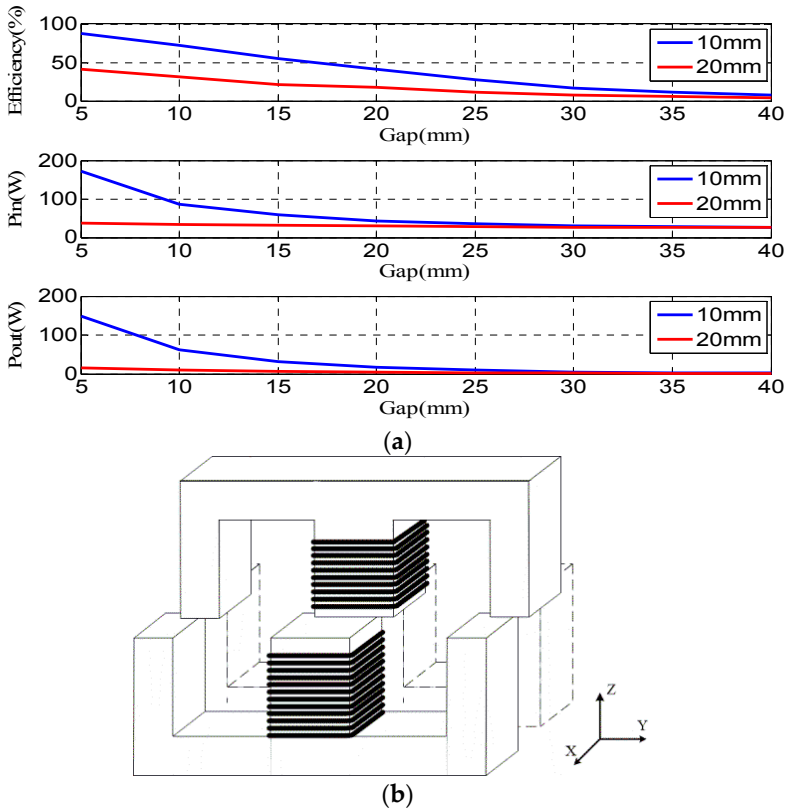

Figure 7. Dislocation effect of the IPT system with varied air gap from 5 mm to 40 mm (fsw: 20 kHz). (**a**) Efficiency, input power; and output power (**b**) Dislocation.

Table 5. Dislocation effect of the IPT system with varied air gap from 5 mm to 40 mm.

Dislocation	Air Gap (mm)	5	10	15	20	25	30	35	40
Dislocation: 10 mm	Efficiency	87.5%	72.1%	54.7%	41.4%	28.1%	17.1%	11%	7.4%
	Input power (W)	171	87	58.5	43.3	36	30	28.5	27
	Output power (W)	147.9	62.7	32	18	10.1	5.1	3.1	2
Dislocation: 20 mm	Efficiency	41.8%	31.2%	21.7%	18.1%	11.8%	8.1%	6.0%	4.4%
	Input power (W)	37.5	34.5	31.5	30	28.5	27	27	25.5
	Output power (W)	15.7	10.8	6.8	5.4	3.3	2.2	1.6	1.1

4.4. Motion

As shown in Figure 4, three H-bridge inverters are connected with each primary E-shaped core and are utilized to transfer power to a secondary E-shaped core. The width of E-shaped core is C = 20 mm (Figure 2b). The space of each primary E-shaped core is 20 mm (Table 4). The three operation modes of three H-bridge inverters are controlled by position regulation sensors. The mode 1H is designed as one H-bridge inverter operated each time; mode 2H, two H-bridge inverters; mode 3H, three H-bridge inverters, respectively. The operating range of mode 1H for each H-bridge inverter is 40 mm without overlap as moving along *X*-axis. The total operating range of mode 1H for three H-bridge inverters is 120 mm. The operating range of mode 2H for each H-bridge inverter is 80 mm as moving along *X*-axis. The nearby two H-bridge inverters are operated with 40 mm overlap. The total operating range of mode 2H for three H-bridge inverters is 160 mm. The operating range of mode 3H for three H-bridge inverters are the same range 140 mm as moving along the *X*-axis.

Figure 8 shows the efficiency, input power, and output power of the IPT system in motion. The air gaps of the IPT system are 10 mm (Figure 8a) and 20 mm (Figure 8b) as moving along the *X*-axis. As shown in Figure 8a,b, comparing modes 1H, 2H, and 3H, the efficiency, input power, and output power of mode 1H vary seriously due to each H-bridge inverter being operated without overlap; the

input power of mode 3H is high, but the efficiency of mode 3H is low due to the wide operating range for three H-bridge inverters; the efficiency, input power, and output power of mode 2H are high and stable due to the adequate overlap operation for three H-bridge inverters. The motion effect of the IPT system as moving along X-axis is given in Table 6 (mode 1H), Table 7 (mode 2H), and Table 8 (mode 3H), respectively. The efficiency, input power, and output power of mode 2H are 76%, 224 W, and 169 W (air gap: 10 mm; *X*-axis: 0 mm) and 51%, 107 W, and 54.1 W (air gap: 20 mm; *X*-axis: 0 mm). Among mode 1H, 2H, and 3H, mode 2H exhibits superior performances of the IPT system and meets the requirements for bus-stop-powered EVs.

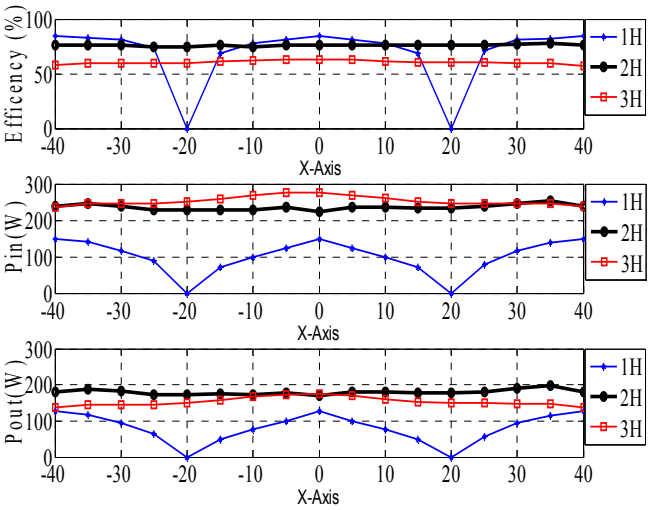

(**a**)

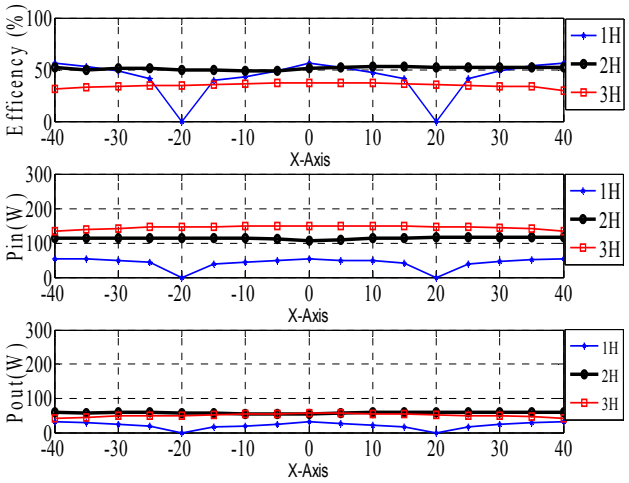

(**b**)

Figure 8. Efficiency, input power, and output power of the IPT system in motion. (**a**) Air gap: 10 mm (**b**) Air gap: 20 mm.

Table 6. Motion effect of the IPT system as moving along *X*-axis; mode 1H (fsw: 20 kHz).

Air Gap	*X*-Axis (mm)	−40	−30	−20	−10	0	10	20	30	40
Air Gap: 10 mm	Efficiency	85%	81%	0%	78%	85%	78%	0%	81%	85%
	Input power (W)	150	117	0	98	150	98	0	117	150
	Output power (W)	128	95	0	77	128	77	0	95	128
Air Gap: 20 mm	Efficiency	56%	49%	0%	43%	56%	43%	0%	49%	56%
	Input power (W)	54	49	0	45	54	45	0	49	54
	Output power (W)	30	24	0	19	30	19	0	24	30

Table 7. Motion effect of the IPT system as moving along *X*-axis; mode 2H (fsw: 20 kHz).

Air Gap	*X*-Axis (mm)	−40	−30	−20	−10	0	10	20	30	40
Air Gap: 10 mm	Efficiency	76%	76%	75%	75%	76%	75%	75%	76%	76%
	Input power (W)	238	240	230	230	224	230	230	240	238
	Output power (W)	181	182	173	173	169	173	173	182	181
Air Gap: 20 mm	Efficiency	52%	51%	50%	49%	51%	49%	50%	51%	52%
	Input power (W)	115	114	114	113	107	113	114	114	115
	Output power (W)	59.4	58.3	57.2	55.1	54.1	55.1	57.2	58.3	59.4

Table 8. Motion effect of the IPT system as moving along *X*-axis; mode 3H (fsw: 20 kHz).

Air Gap	*X*-Axis (mm)	−40	−30	−20	−10	0	10	20	30	40
Air Gap: 10 mm	Efficiency	58.1%	59.4%	59.7%	62.4%	63.0%	62.4%	59.7%	59.4%	58.1%
	Input power (W)	237	246	250.5	268.5	277.5	268.5	250.5	246	237
	Output power (W)	137.8	146.2	149.6	167.4	174.8	167.4	149.6	146.2	137.8
Air Gap: 20 mm	Efficiency	31.3%	33.7%	34.4%	36.1%	37.5%	36.1%	34.4%	33.7%	31.3%
	Input power (W)	135	142.5	145.5	150	150	150	145.5	142.5	135
	Output power (W)	42.3	48.0	50.0	54.1	56.2	54.1	50.0	48.0	42.3

Figure 9 shows the waveforms of the P topology IPT system operated at mode 1H. As shown in Figure 4b, the X-Z table is utilized to move the secondary E-shaped core along the *X*-axis at a speed of 16.7 cm/s. The time intervals of T1, T2, and T3 are 0.24 s. The mode 1H is designed as one H-bridge inverter operated at each time interval. Therefore, voltage (v_s) and current (i_s) waveforms of the IPT system are varied seriously.

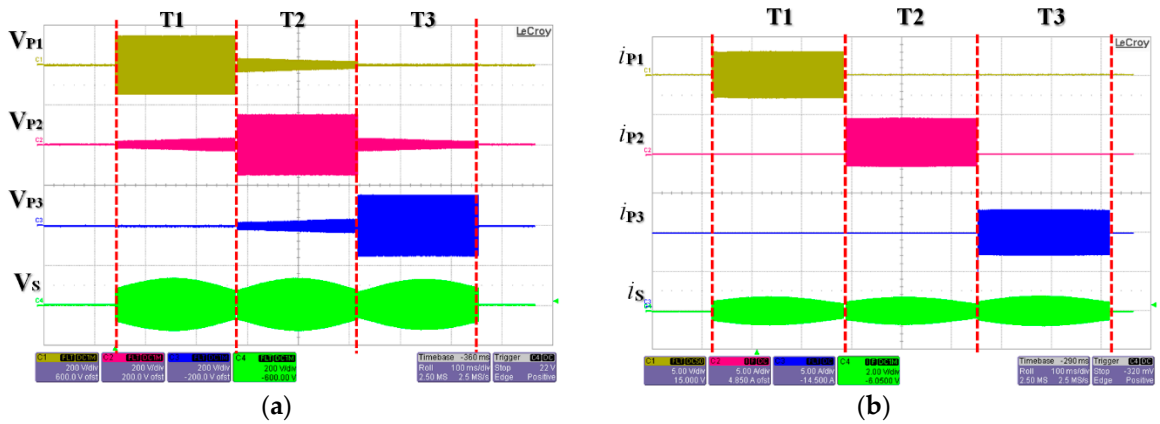

Figure 9. Waveforms of the P topology IPT system operated at mode 1H (air gap: 10 mm; time: 100 ms/div.; voltage: 200 v/div.; current i_{p1}, i_{p2}, and i_{p3}: 5 A/div.; current i_s: 2 A/div.). (**a**) Voltages; (**b**) Currents.

Figure 10 shows the waveforms of the P topology IPT system operated at mode 2H (speed: 16.7 cm/s). The time intervals of T1, T2, T3, and T4 are 0.24 s. The voltage (v_s) and current (i_s) waveforms of mode 2H are high and stable due to the adequate overlap operation for three H-bridge inverters. Compared Figure 10 (mode 2H) with Figure 9 (mode 1H), mode 2H exhibits high efficiency 76%, stable input power and output power. Therefore, the P topology IPT system operated at mode 2H is validated to meet the requirements for bus-stop-powered EVs.

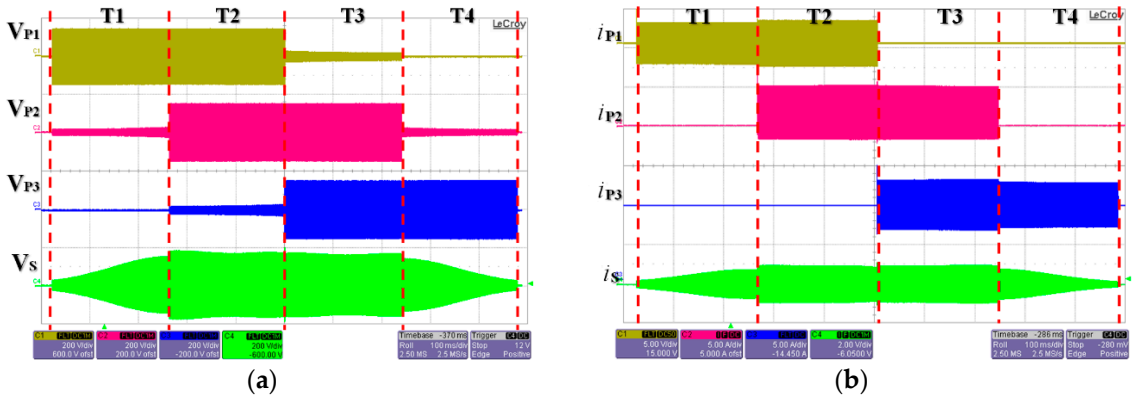

Figure 10. Waveforms of the P topology IPT system operated at mode 2H (air gap: 10 mm; time: 100 ms/div.; voltage: 200 v/div.; current i_{p1}, i_{p2}, and i_{p3}: 5 A/div.; current i_s: 2 A/div.) (**a**) Voltages; (**b**) Currents.

5. IPT System Operated at Large Air Gap

The IPT system operated at large air gap is restricted by the EE-shaped ferrite cores used. Therefore, finite element analysis (FEA) software is utilized to validate the performances of the proposed scheme. Figure 11 shows the IPT system based on the FEA software. According to Figure 2b, and Figure 11a which shows the 3D model of the EE-shaped ferrite cores, the dimensions are A (760 mm), B (30 mm), C (760 mm), D (20 mm), E (720 mm), F (40 mm), G (F/2), H (E/2–F/2), and I (A/4–E/4). The air gap between the EE-shaped cores is 150 mm. The material of the EE-shaped cores is 3C90 made by Ferroxcube. Figure 11b shows the circuit of the SP topology based on the FEA software. The primary and secondary excitation windings are 11 turns and 11 turns, respectively. The primary and secondary inductances are L_p (147 μH) and L_s (147 μH). The primary series capacitor and secondary parallel capacitor are C_p (0.43 μF) and C_s (0.43 μF). Therefore, the resonant frequency is designed as 20 kHz.

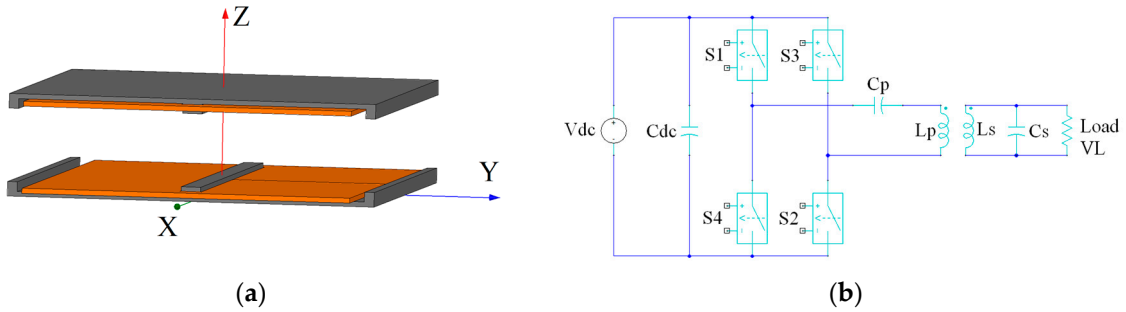

Figure 11. IPT system based on finite element analysis (V_{dc}: 300 V; fsw: 20 kHz; air gap: 150 mm). (**a**) 3D Model of EE-shaped ferrite cores; (**b**) Circuit of the SP topology.

Figure 12a,b show the waveforms of the SP topology IPT system based on FEA. As shown in Figure 12a, the input voltage is a square wave with amplitude 300 V and the output voltage is a sinusoidal wave with amplitude 793 V. The amplitudes of the input current and output current are 41 A and 43 A as shown in Figure 12b. The efficiency, input power, and output power of the SP topology IPT system are 80%, 3930 W, and 3136 W, respectively.

Figure 12c,d show the waveforms of the P topology IPT system based on FEA. As shown in Figure 12c, the input voltage is a square wave with amplitude 300 V and the output voltage is a sinusoidal wave with amplitude 432 V. The amplitudes of the input current and output current are 25.5 A and 23 A as shown in Figure 12d. The efficiency, input power, and output power of the

P topology IPT system are 59.8%, 1560 W, and 934 W, respectively. Comparing the SP topology (Figure 12a,b) with the P topology (Figure 12c,d), the IPT system adopting a SP topology exhibits superior performances under large (150 mm) air gap conditions.

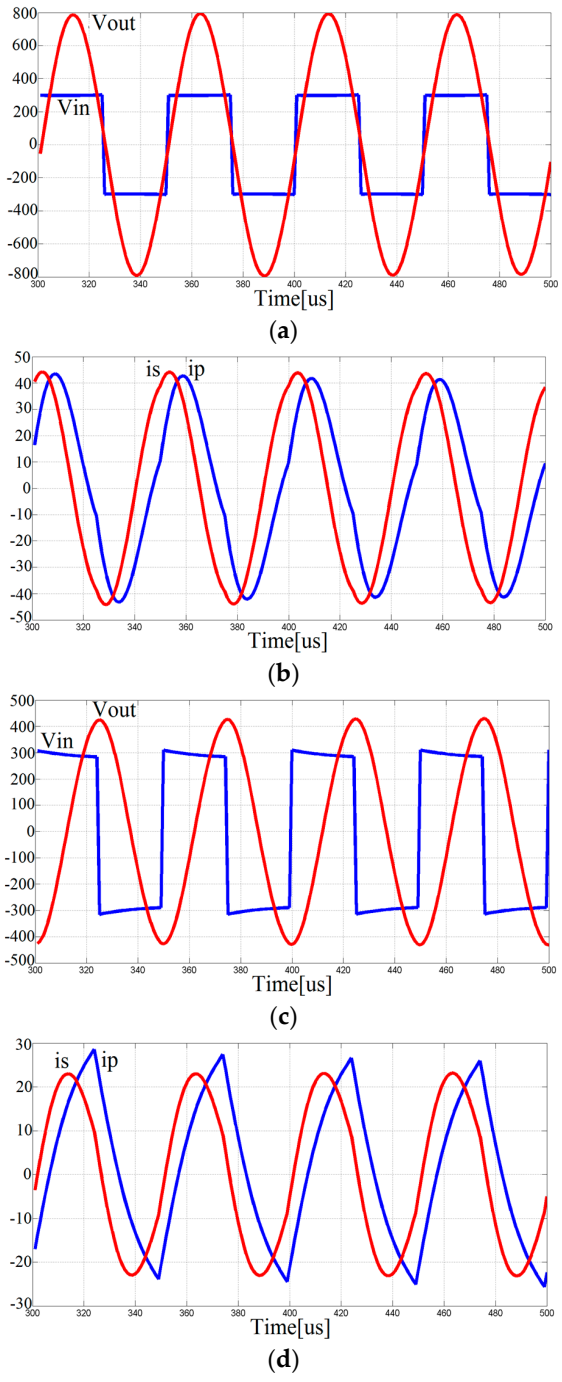

Figure 12. Waveforms of the IPT system based on finite element analysis (V_{dc}: 300 V; fsw: 20 kHz; air gap: 150 mm). (**a**) Input and output voltages of SP topology; (**b**) Input and output currents of SP topology; (**c**) Input and output voltages of P topology; (**d**) Input and output currents of P topology.

6. Conclusions

This study discusses the IPT system based on EE-shaped ferrite cores. The transfer function and frequency response of the SP topology and P topology IPT systems are presented. The SP topology

is suitable for large air gaps and the P topology is suitable for small air gaps. The issues of the IPT system such as efficiency, air gap, displacement, dislocation, and motion are discussed. Finite element analysis is utilized to validate the SP topology IPT system operated under large air gap conditions. Furthermore, multi-H-bridge inverters are utilized to increase the transfer power of the IPT system. The three operation modes (1H, 2H, and 3H) of three H-bridge inverters are controlled by position regulation sensors. Among mode 1H, 2H, and 3H, mode 2H exhibits superior performance in the IPT system and meets the requirements for bus-stop-powered EVs.

Acknowledgments: This work was supported by the Ministry of Science and Technology of R.O.C. under grant MOST 103-2221-E-216-008.

Author Contributions: Chung-Chuan Hou modeled the system, analyzed the experimental data, wrote the draft and revised the paper; Kuei-Yuan Chang established the experimental platform, measured and analyzed the experimental data.

Conflicts of Interest: The authors declare no conflict of interest.

References

1. Miller, J.M.; Onar, O.C.; Chinthavali, M. Primary-side power flow control of wireless power transfer for electric vehicle charging. *IEEE J. Emerg. Sel. Top. Power Electron.* **2015**, *3*, 147–162. [CrossRef]
2. Wang, C.; Stielau, O.H.; Covic, G.A. Design considerations for a contactless electric vehicle battery charger. *IEEE Trans. Ind. Electron.* **2005**, *52*, 1308–1314. [CrossRef]
3. Li, S.; Mi, C.C. Wireless power transfer for electric vehicle applications. *IEEE J. Emerg. Sel. Top. Power Electron.* **2015**, *3*, 4–17.
4. Choi, S.Y.; Gu, B.W.; Jeong, S.Y.; Rim, C.T. Advances in wireless power transfer systems for roadway-powered electric vehicles. *IEEE J. Emerg. Sel. Top. Power Electron.* **2015**, *3*, 18–36. [CrossRef]
5. Zhang, W.; Wong, S.; Tse, C.K.; Chen, Q. An optimized track length in roadway inductive power transfer systems. *IEEE J. Emerg. Sel. Top. Power Electron.* **2014**, *2*, 598–608. [CrossRef]
6. Shin, J.; Shin, S.; Kim, Y.; Ahn, S.; Lee, S.; Jung, G.; Jeon, S.; Cho, D. Design and implementation of shaped magnetic-resonance-based wireless power transfer system for roadway-powered moving electric vehicles. *IEEE Trans. Ind. Electron.* **2014**, *61*, 1179–1192. [CrossRef]
7. Chen, L.; Nagendra, G.R.; Boys, J.T.; Covic, G.A. Double-coupled systems for IPT roadway applications. *IEEE J. Emerg. Sel. Top. Power Electron.* **2015**, *3*, 37–49. [CrossRef]
8. Nagendra, G.R.; Chen, L.; Covic, G.A.; Boys, J.T. Detection of EVs on IPT highways. *IEEE J. Emerg. Sel. Top. Power Electron.* **2014**, *2*, 584–597. [CrossRef]
9. Kurs, A.; Karalis, A.; Moffatt, R.; Joannopoulos, J.D.; Fisher, P.; Soljacic, M. Wireless power transfer via strongly coupled magnetic resonances. *Science* **2007**, *317*, 83–86. [CrossRef] [PubMed]
10. Zhang, W.; Wong, S.; Tse, C.K.; Chen, Q. Analysis and comparison of secondary series- and parallel-compensated inductive power transfer systems operating for optimal efficiency and load-independent voltage-transfer ratio. *IEEE Trans. Power Electron.* **2014**, *29*, 2979–2990. [CrossRef]
11. Aldhaher, S.; Luk, P.C.; Whidborne, J.F. Electronic tuning of misaligned coils in wireless power transfer systems. *IEEE Trans. Power Electron.* **2014**, *29*, 5975–5982. [CrossRef]
12. Pantic, Z.; Lee, K.; Lukic, S.M. Multifrequency inductive power transfer. *IEEE Trans. Power Electron.* **2014**, *29*, 5995–6005. [CrossRef]
13. Pinuela, M.; Yates, D.C.; Lucyszyn, S.; Mitcheson, P.D. Maximizing dc-to-load efficiency for inductive power transfer. *IEEE Trans. Power Electron.* **2013**, *28*, 2437–2447. [CrossRef]
14. Musavi, F.; Eberle, W. Overview of wireless power transfer technologies for electric vehicle battery charging. *IET Power Electron.* **2013**, *7*, 60–66. [CrossRef]